

# Northumbria Research Link

Citation: Zhang, Shaobin, Chen, Xue, Moumni, Ziad and He, Yongjun (2018) Coexistence and compatibility of martensite reorientation and phase transformation in high-frequency magnetic-field-induced deformation of Ni-Mn-Ga single crystal. International Journal of Plasticity, 110. pp. 110-122. ISSN 0749-6419

Published by: Elsevier

URL: <http://dx.doi.org/10.1016/j.ijplas.2018.06.010>  
<<http://dx.doi.org/10.1016/j.ijplas.2018.06.010>>

This version was downloaded from Northumbria Research Link:  
<http://nrl.northumbria.ac.uk/id/eprint/35714/>

Northumbria University has developed Northumbria Research Link (NRL) to enable users to access the University's research output. Copyright © and moral rights for items on NRL are retained by the individual author(s) and/or other copyright owners. Single copies of full items can be reproduced, displayed or performed, and given to third parties in any format or medium for personal research or study, educational, or not-for-profit purposes without prior permission or charge, provided the authors, title and full bibliographic details are given, as well as a hyperlink and/or URL to the original metadata page. The content must not be changed in any way. Full items must not be sold commercially in any format or medium without formal permission of the copyright holder. The full policy is available online: <http://nrl.northumbria.ac.uk/policies.html>

This document may differ from the final, published version of the research and has been made available online in accordance with publisher policies. To read and/or cite from the published version of the research, please visit the publisher's website (a subscription may be required.)



# Coexistence and compatibility of martensite reorientation and phase transformation in high-frequency magnetic-field-induced deformation of Ni-Mn-Ga single crystal

Shaobin Zhang<sup>a</sup>, Xue Chen<sup>b</sup>, Ziad Moumni<sup>a, c</sup>, Yongjun He<sup>a, \*</sup>

<sup>a</sup> IMSIA, UMR 8193 CNRS-EDF-CEA-ENSTA, Université Paris Saclay, 828 Boulevard des Maréchaux, 91762 Palaiseau Cedex, France

<sup>b</sup> Faculty of Engineering and Environment, Northumbria University, Newcastle upon Tyne NE1 8ST, UK

<sup>c</sup> State IJR Center of Aerospace Design and Additive Manufacturing, Northwestern Polytechnical University, Xian, Shaanxi 710072, China

## ARTICLE INFO

### Keywords:

Ferromagnetic shape memory alloys  
High-frequency magnetic actuation  
Microstructure compatibility  
Instability of strain oscillation  
Thermo-magneto-mechanical coupling

## ABSTRACT

High-frequency magnetic-field-induced Martensite Reorientation (MR) is one of the most important advantages of Ferromagnetic Shape Memory Alloys (FSMAs), but its stability is threatened by dissipation heat accumulation ("self-heating") of cyclic frictional twin-boundary motion, which can cause temperature-induced Phase Transformation (PT) and reduce the output-strain amplitude significantly. In this paper, the interaction of the temperature-induced PT and the magnetic-field-induced MR during high-frequency magnetic actuation on FSMA is studied with in-situ observations of local-strain evolution in conjunction with microstructure-compatibility analysis. Based on the nominal strain and temperature responses and the corresponding local-strain maps, it is revealed that, when the temperature-induced PT takes place during the high-frequency field-induced MR, the specimen is divided into three zones: **non-active austenite zone** (with a constant deformation), **active martensite zone** (with cyclic deformations of MR) and **buffering needle zone** (interfacial zone) with a fine-needle-twin structure which plays an important role in maintaining the compatibility between austenite and martensite zones with different cyclic deformations during the dynamic loading. A novel mechanism is revealed that, under the magnetic actuation with changing ambient airflow, the "self-heating" **temperature-driven phase boundary motion** and the **magnetic-field-driven twin boundary motion** can coexist, because the specimen needs to self-organize the different phases/variants to satisfy all the thermo-magneto-mechanical boundary conditions. Taking advantage of this mechanism, the volume fractions of austenite and martensite zones can be adjusted with changing ambient airflow velocity, which provides an effective way to tune the nominal output-strain amplitude (from 1% to 6% in the current study) while the working temperature is kept almost constant (around  $M_s$  and  $M_f$ ).

\* Corresponding author.

Email address: [yongjun.he@ensta-paristech.fr](mailto:yongjun.he@ensta-paristech.fr) (Y. He)

## 1. Introduction

Ni-Mn-Ga single crystal is a typical Ferromagnetic Shape Memory Alloy (FSMA) which has potential applications such as magneto-caloric refrigerators (Basso, 2011; Li et al., 2014; Singh et al., 2014; Sokolovskiy et al., 2014) and high-frequency large-stroke actuators (Henry, 2002; Smith et al., 2014; Techapiesancharoenkij et al., 2009; Yin et al., 2016) based on the field-induced martensitic phase transformation (transformation between martensite and austenite phases) and the field-induced martensite reorientations (transition among the variants of the martensite phase), respectively. It was reported in the literature that the levels (magnitudes) of the magnetic fields required to drive the Phase Transformation (PT) and the Martensite Reorientation (MR) are significantly different: several Teslas for the phase transformation while less than 1 Tesla for the martensite reorientation (Bruno et al., 2016; Haldar et al., 2014; Karaca et al., 2006, 2009). So most of the existing research work studied phase transformation (Arndt et al., 2006; Karaca et al., 2009; Rogovoy and Stolbova, 2016; Sehitoglu et al., 2012) and martensite reorientation (Heczko et al., 2000; Karaca et al., 2006; Lai et al., 2008; Straka et al., 2006) separately without considering their interactions.

While the magnetic-field-driven phase transformation needs a very strong magnetic field (which is not easy to obtain), the temperature-induced phase transformation can be easily triggered in FSMA by external heat sources (Pinneker et al., 2014) or the self-heating due to the intrinsic dissipation of the cyclic martensite reorientation. For example, the self-heating induced temperature increasing rate during the first 20 s of actuation is around  $0.5^\circ\text{C/s}$  in (Pascan et al., 2015) and  $0.3^\circ\text{C/s}$  in (Lai, 2009). Particularly, in a high-frequency FSMA actuator, the dissipation heat of the cyclic frictional twin boundary motion during the martensite reorientation can be accumulated quickly to increase the specimen temperature to a level comparable with the material characteristic phase-transformation temperatures where the Martensite-to-Austenite (M-to-A) phase transformation can take place (Jugo et al., 2017; Pascan, 2015; Zhang et al., 2018). The phase transformation disturbs the process of the field-induced martensite reorientation, leading to a significant drop in the output strain amplitude of the FSMA actuators (Jugo et al., 2017; Pascan, 2015; Zhang et al., 2018). This instability problem is obviously harmful in developing high-frequency large-stroke FSMA actuators.

Recently, a method of changing the ambient airflow (governing the heat exchange efficiency) to control the specimen working temperature was proposed in (Zhang et al., 2018) to overcome this difficulty and to achieve a large output strain in the high-frequency actuation as shown in Fig. 1, where the combination of the orthogonal mechanical force and the cyclic magnetic field leads to the cyclic switching between the two different martensite variants (so-called “stress-preferred variant”  $M_1$  and “field-preferred variant”  $M_2$ ). It was shown that the output strain amplitude depended on the controlled ambient airflow velocity. Particularly, when the temperature-induced phase transformation and the field-induced martensite reorientation coexist, the working temperature of the specimen consisting of different phases and variants was kept almost constant (close to the material characteristic phase transformation temperatures) while the output strain amplitude changed significantly from 6% (complete martensite reorientation) to less than 1% (only little martensite reorientation), depending on the airflow velocity. One possible explanation for this phenomenon is that the specimen could self-organize its volume fractions of the Martensite phase (M-phase) and the Austenite phase (A-phase) to satisfy the thermal balance between the martensite-reorientation dissipation heat and the heat transfer to the ambient (controlled by the airflow velocity) (Zhang et al., 2018). To verify this conjecture, a high-frequency magnetic actuation on  $\text{Ni}_2\text{MnGa}$  single crystal is performed under an ambient airflow with stepped changing velocities (to change the heat-exchange efficiency), and in-situ Digital Image Correlation (DIC) observation on local strain distributions and evolutions is conducted in the current study. It is found that the temperature-induced

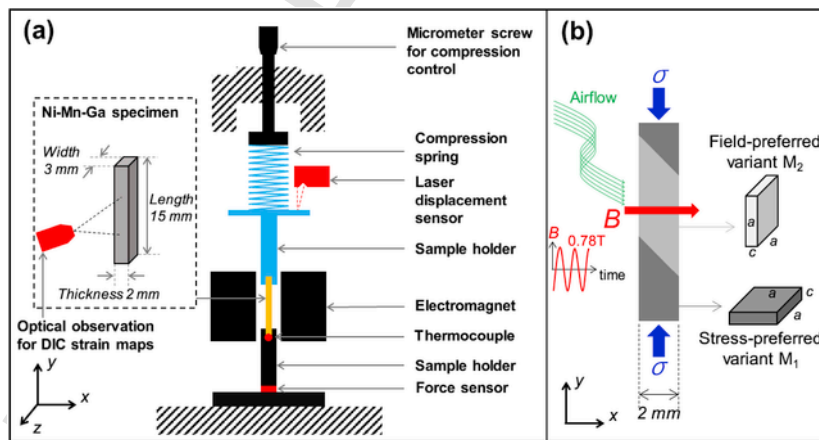


Fig. 1. Schematic of the actuation system.

M-to-A phase transformation makes the specimen form **non-active austenite zone** (A-phase with a constant strain) and **active martensite zone** (M-phase with 6% strain oscillation due to cyclic martensite reorientation) during the magnetic actuation, and the volume fractions of the non-active and active zones change significantly under the different ambient airflow velocities. This reveals a novel mechanism that both the **temperature-driven phase boundary motion** and the **magnetic-field-driven twin boundary motion** can be activated simultaneously during the high-frequency magnetic actuation on FSMA, which enables the specimen to self-organize the different phases/variants to satisfy all the thermo-magneto-mechanical boundary conditions and provides an effective option to tune the high-frequency output strain amplitude of FSMA (from 1% to 6% in the current study).

Moreover, the in-situ observations on the local strain evolution demonstrate how the active zone (with the strain oscillation of the cyclic martensite reorientation) is compatible with the non-active zone (with a constant strain of the A-phase). The compatibility between different phases (and different variants) in shape memory alloys has been widely studied (Bhattacharya, 2003; Seiner et al., 2011; Stupkiewicz et al., 2007); the compatibility analyses are based on the principle of the energy minimization studying the **static** configurations: only some discrete phase/variants fractions satisfy the compatibility. In other words, the phase/variants fractions can't continuously change in the compatible configurations. (Note: some special materials satisfying so-called "co-factor conditions" might allow a continuous change in the compatible phase fractions (Chen et al., 2013; Song et al., 2013)). To the authors' best knowledge, the currently-observed compatibility between the active martensite zone of strain oscillation (with the cyclic and continuous change in the volume fractions of the two martensite variants ( $M_1$  and  $M_2$ )) and the non-active austenite zone of a static strain has never been explained in the literature. In this paper, based on the observations of the distributions of the phases/variants and the microstructure compatibility analysis, it is revealed that, for the compatibility between the active martensite zone and non-active austenite zone, the interface between the two zones is not a sharp habit plane, but a buffering zone with needle-like fine twins where the third martensite variant  $M_3$  (which doesn't participate in the cyclic martensite reorientation) might be generated during the self-organizing process of the simultaneous field-induced martensite reorientation and the temperature-induced phase transformation.

## 2. Material properties and experiment setup

In this study, a rectangular bar of  $\text{Ni}_{50}\text{Mn}_{28}\text{Ga}_{22}$  (at. %) single crystal with dimensions in  $2 \times 3 \times 15$  mm (from ETO Magnetic GmbH) is used in the experiments, as shown in Fig. 1. The material characteristic transformation temperatures  $M_s$ ,  $M_f$ ,  $A_s$  and  $A_f$  were obtained as  $36.5^\circ\text{C}$ ,  $35.5^\circ\text{C}$ ,  $41.5^\circ\text{C}$  and  $42.2^\circ\text{C}$ , respectively, from a DSC (differential scanning calorimetry) test detailed in Appendix A. The material is in the state of 10M martensite phase at room temperature and the martensite variants are slightly monoclinic ( $\gamma = 90.37^\circ$ ). For the simplicity of the analysis here, we assume that the martensite variants are tetragonal with two long axes "a" and one short axis "c" (as adopted in various researches (Haldar et al., 2014; Karaca et al., 2006, 2007, Pinneker et al., 2014, 2013)). The spontaneous magnetization is along the short axis "c" for the studied material. Accompanied by the field-induced martensite reorientation between variants with different orientations of short axis "c", the material's magnetization direction rotates (some typical magnetization measurements can be found in (Ge et al., 2005; Henry, 2002; Murray et al., 2000)). The high-temperature austenite phase is  $\text{L}2_1$  cubic with a lattice constant of  $a_0$ . The typical lattice parameters are  $a \approx 0.595\text{nm}$  and  $c \approx 0.561\text{nm}$  for the 10M martensite and  $a_0 \approx 0.584\text{nm}$  for the cubic austenite (Heczko et al., 2002; Murray et al., 2000; Pinneker et al., 2014, 2013; Straka et al., 2008). All faces of the rectangular bar are cut approximately along the  $\{100\}$  planes of the parent cubic austenite by the supplier.

Before the test, the specimen is fully compressed along y-direction to obtain the single variant state with the short-axis (c-axis) along y-direction (so-called stress-preferred variant, shown as  $M_1$  in Fig. 1(b)), which is the reference state for the calculation of the specimen deformation strain in this paper. At the beginning of the test, an initial compressive stress  $\sigma_{ini} = 0.4\text{MPa}$  is applied on the specimen along y-direction by a compressed spring (of stiffness  $5.5\text{kN/m}$ ), as shown in Fig. 1. Then a magnetic field (with magnetic flux density  $B$  cyclically varying between  $\pm 0.78$  Tesla as shown in Fig. 1(b)) of frequency  $f_{mag} = 90\text{Hz}$  is applied horizontally along x-direction to drive the martensite reorientation from  $M_1$  to  $M_2$  (so-called field-preferred variant with the short axis c along x-direction) as shown in Fig. 1(b). The martensite reorientation makes the specimen length  $L_y$  change, which leads to a change in the compressive stress applied by the spring. The competition between the cyclic magnetic field and the evolving compressive stress eventually drives the cyclic martensite reorientation between the variants  $M_1$  and  $M_2$ , which produces cyclic strain along y-direction. The nominal output strain along y-direction is measured by a laser displacement sensor (Keyence LK-H027) at the upper specimen holder. Theoretically, the strain along y-direction is around 6% for the martensite reorientation from  $M_1$  to  $M_2$  ( $(a_0 - c)/c \approx 6\%$ ), and around 4% for the phase transformation from  $M_1$  to the cubic austenite ( $(a_0 - c)/c \approx 4\%$ ). It is noted that the lattice parameters are temperature dependent (Glavatska et al., 2002; Pagounis et al., 2014; Straka et al., 2006), so the strain value is also temperature dependent. But in the current experiments with the small temperature variation (i.e., from the room temperature ( $\approx 18^\circ\text{C}$ ) to the martensite start temperature  $M_s = 36.4^\circ\text{C}$ ), the temperature effect on the lattice parameters can be ignored. During the test, the ambient heat-ex-

change condition is controlled by forcing ambient airflow (around the room temperature) of velocity  $v_{air}$  changing from 0 m/s to 16 m/s to pass through the specimen (see Fig. 2(a)). The specimen temperature is monitored by a thermocouple (K-type, 0.5 mm sheath diameter) at the bottom end of the specimen. During the whole dynamic actuation, a CMOS camera of 2048×1088 pixels (Basler acA2000-340 km) with Nikkor lens is used to record the optical images of the specimen surface (in a gage section of around 4 mm), which are processed by Digital Image Correlation (DIC) software Vic-2D (Correlated Solutions) to obtain the in-situ local strain distributions and evolutions under different airflow velocities.

### 3. Experimental results

Fig. 2(a) shows the loading conditions (the cyclic magnetic field between  $\pm 0.78$  Tesla and the changing airflow velocity ( $v_{air} = 0$  m/s  $\sim$  16 m/s)) and the responses of the nominal output strain and the specimen temperature, while Fig. 2(b) shows the zoomed nominal strain curves and the local strain distributions (DIC strain maps) of the corresponding responses at several typical time slots ( $t_1 \sim t_7$ ). It is seen that at each increase in the airflow velocity, the amplitude  $\Delta\epsilon$  of the strain oscillation increases correspondingly (see the strain amplitude change at the time  $t \approx 100$ s,

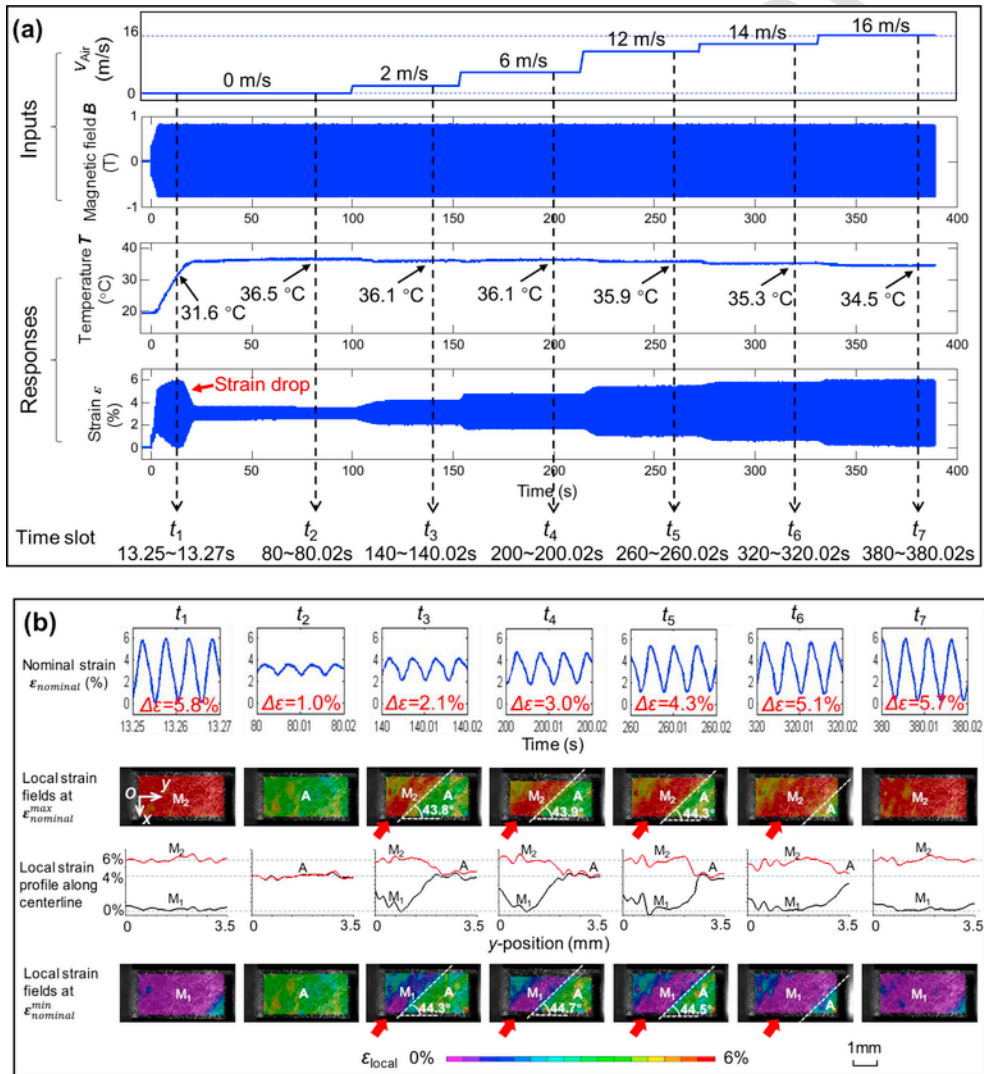


**Fig. 2.** (a) The global responses of FSMA-actuator under the same magnetic loading (the cyclic magnetic field between  $\pm 0.78$  Tesla) but the changing airflow velocity ( $v_{air} = 0$  m/s  $\sim$  16 m/s). (b) The zoomed nominal strain curves, the DIC local strain maps and the corresponding local strain profiles (the red and black lines represent the local strains at the maximum and minimum nominal strain states respectively) along the centerline at the typical time slots marked in (a). (For interpretation of the references to color in this figure legend, the reader is referred to the Web version of this article.)



155 s, 220 s, 275 s, and 330 s in Fig. 2(a) and the zoomed nominal strain curves at different time slots in Fig. 2(b)). However, a strain amplitude drop from 5.8% to 1.0% is observed at  $t \approx 15$  s even though the ambient airflow didn't change (keeping still air,  $v_{air} = 0$  m/s).

With the start of the dynamic test in still air ( $v_{air} = 0$  m/s at  $t = 0$  in Fig. 2(a)), the output strain amplitude increased rapidly to be close to the strain (6%) of a complete martensite reorientation while the specimen temperature  $T$  increased slowly from the room temperature, for example,  $T$  increased to  $31.6^\circ\text{C}$  at  $t = 13.25$  s in Fig. 2(a). The corresponding DIC strain maps at the time slot  $t_1$  (13.25 s–13.27 s) in Fig. 2(b) show that the optically observed gauge section of the specimen had the local strains of around 0% (with the violet color) and around 6% (with the red color) when the nominal output strain (the global strain of the whole specimen) reached the minimum and maximum levels, respectively. That means a complete martensite reorientation cycle can be achieved at that time. The local strain evolution of a typical cycle at the time slot  $t_1$  is shown in Fig. 3 where the twin boundary (interface between the two martensite variants) of an angle of  $44.7^\circ$  at the  $x$ - $y$  plane (the observed specimen surface) can be identified. It should be noted that, during the magnetic loading, many fine twins can be generated and the motion of numerous twin boundaries can be activated (Chmielus et al., 2008; Lai et al., 2008). In the current test, the detailed microstructures of such fine twins cannot be resolved due to the limited resolution of the optical camera. So the fine-twin regions are just denoted by  $M_1 + M_2$  domains whose strain can continuously change between 0% and 6% as shown in the local strain profiles along the center line of the gauge section in Fig. 3.

The observation above clearly demonstrates that a complete martensite reorientation cycle with 6% strain amplitude can be achieved under the current magnetic actuation. But the specimen temperature  $T$  kept increasing at  $t_1$  as shown in Fig. 2(a), which indicates that the system had not yet reached a steady state. When the specimen temperature became higher than  $36^\circ\text{C}$  (close to the material characteristic phase transformation temperatures), the output strain amplitude  $\Delta\epsilon$  dropped to around 1% at  $t \approx 20$  s in Fig. 2(a). After the strain drop, the system reached a steady state—both the strain amplitude and temperature were kept almost constant ( $\Delta\epsilon = 1.0\%$  and  $T = 36.5^\circ\text{C}$ ). The typical local strain fields at this stage (time slot  $t_2$  of 80 s–80.02 s in Fig. 2(b)) show almost the same strain level of around 4% (represented by the green color) in the observed region of the specimen for both the minimum and maximum nominal strain of the cycle. This indicates that the observed gauge section of the specimen contributes little to the output strain during the cyclic magnetic loading. The green region is occupied by the austenite phase (A-phase) for the following facts: (a) the theoretical strain of the cubic A-phase with respect to the martensite variant  $M_1$  is around 4% for the material (as calculated in Section 2), (b) the green region is not sensitive to such low level of magnetic

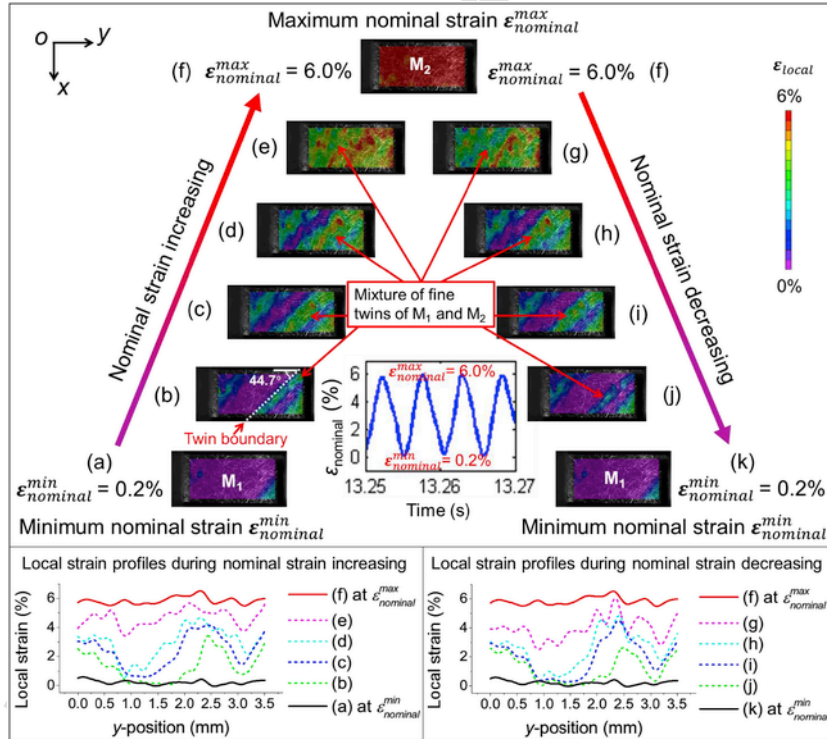


Fig. 3. DIC local strain evolutions in a typical cycle of the martensite reorientation process before the occurrence of the strain drop phenomenon (pure martensite phase) at the time slot  $t_1$ .

field ( $<1$  Tesla), and (c) the green region appears when the specimen temperature was increased to the material characteristic phase transformation temperatures. Thus, the field-induced deformation of martensite reorientation was significantly suppressed due to the “self-heating” temperature-induced phase transformation.

When the ambient airflow velocity was increased to 2 m/s, the temperature decreased slightly from 36.5 °C to 36.1 °C; but the nominal output strain amplitude increased significantly from 1.0% to 2.1%, as shown in Fig. 2(a) and the zoomed nominal strain curve at  $t_3$  (140 s–140.02 s) in Fig. 2(b). The corresponding DIC strain maps at  $t_3$  in Fig. 2(b) demonstrate that, in the observed gauge section, the Martensite zone (M-zone) of cyclic martensite reorientation (where the local strain oscillated between 0% and 6%, as marked by red arrows) appeared again and the volume of the A-phase (A-zone, as shown in green) was reduced. The interface between the A-zone and the M-zone (A-M phase boundary) with an angle near 45° can be identified (see dashed lines in Fig. 2(b)). Further increasing the airflow velocity made the nominal output strain amplitude increase and the volume of the A-phase decrease (through the phase boundary propagation) as shown by the nominal output strain evolution ( $\Delta\epsilon = 2.1\%$ , 3.0%, 4.3% and 5.1%) and the DIC strain maps at  $t_3 \sim t_6$  in Fig. 2(b). It is seen from the local strain field evolutions from  $t_3$  to  $t_6$  that the phase boundary between A- and M-zones propagated with the increasing airflow velocity and kept the same angle (near 45°), which means that changing the ambient heat-exchange efficiency (by changing airflow velocity) can drive the A-M phase boundary motion to adjust the volume fractions of A- and M-zones. Fig. 4 shows a typical cycle of the local strain evolution for the time slot  $t_6$ . By comparing the DIC strain maps at the minimum nominal strain ( $\epsilon_{nominal}^{min} = 0.6\%$ ) and the maximum nominal strain ( $\epsilon_{nominal}^{max} = 5.7\%$ ), we can identify the active zone (i.e., M-zone with cyclic strain due to martensite reorientation between  $M_1$  and  $M_2$ ) and the non-active zone (i.e., A-phase with constant local strain). It is interesting to note that the A-M phase boundary (represented by dashed lines) between the active M-zone and the non-active A-zone is nearly parallel to the twin boundary (represented by dotted lines) at the observed surface (x-y plane), and both of them have an angle of around 45°. It is further noted that the A-M phase boundary is fixed while the twin boundaries cyclically move in the active M-zone in the magnetic loading cycle.

At the time slot  $t_6$ , the output strain  $\Delta\epsilon$  was 5.1% and there still existed A-phase (non-active zone) in the specimen. In order to improve the output strain, the airflow was further increased to 16 m/s where  $\Delta\epsilon$  increased to 5.7% as shown by the strain response and the DIC strain maps in the time slot  $t_7$  (380 s–380.02 s) in Fig. 2(b). It is seen that, in the observed gauge section, the non-active zone (A-phase) disappeared; the whole gauge section took a cyclic complete martensite reorientation between martensite variants  $M_1$  and  $M_2$ .

In summary, the temperature-induced Martensite-to-Austenite (M-to-A) phase transformation occurred to disturb the field-induced deformation of the martensite reorientation, leading to a significant strain drop, when the specimen temperature increased to the material characteristic phase transformation temperature due to the frictional twin

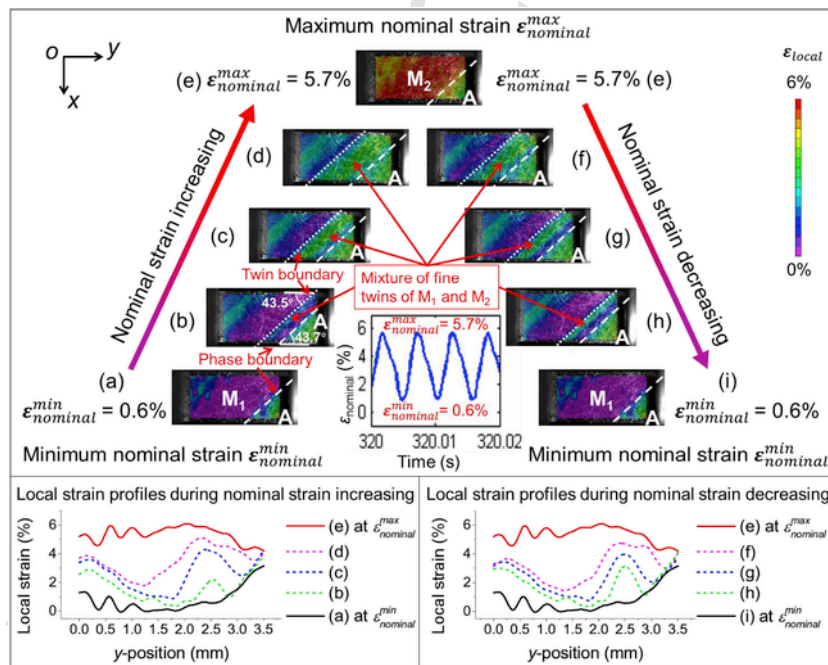


Fig. 4. DIC local strain evolutions in a typical cycle of the martensite reorientation process with the existence of the non-active A-phase (the green region of A-phase (at lower right corner in each DIC map) has a constant local strain around 4%) at the time slot  $t_6$ . (For interpretation of the references to color in this figure legend, the reader is referred to the Web version of this article.)

boundary motion. The evolution of the DIC local strain maps reveals that the volume fraction of the A-phase (non-active zone contributing little to the cyclic output strain) in the specimen significantly changed with the ambient airflow velocity. That is to say, the coexistence of the temperature-driven phase boundary motion (phase transformation) and the magnetic-field-driven twin boundary motion (martensite reorientation) is possible by controlling the external magnetic field and the ambient airflow simultaneously. This new phenomenon poses some critical questions in theoretical understanding:

- (1) As the M-to-A phase transformation is triggered by the temperature rise, it is normally expected that the stable working temperature during the coexistence of the field-induced martensite reorientation and the temperature-induced phase transformation should be close to  $A_s$  and  $A_f$ . However, both the previous study (Zhang et al., 2018) and the current experiment (Fig. 2(a)) show that the stable working temperature is around  $M_s$  and  $M_f$ . It is noted that the measured temperature at a single point in the current test can only roughly describe the global temperature evolution of the specimen. To reveal the local temperature distribution (particularly near the twin/phase boundaries) during the actuation, precise full-field temperature measurement and delicate dynamic modeling are needed.
- (2) The cyclic local strain evolutions (Figs. 3 and 4) show that the non-active A-zone (A-phase with constant deformation) can be compatible with the active M-zone (with cyclic deformation and varying fractions of martensite variants). Such compatibility is not expected because normally the A-phase (cubic phase) can only be compatible with martensite (tetragonal phase) twins of some specified variant fractions which satisfy the energy minimization, i.e., A-phase cannot be compatible with a single martensite variant or martensite twins with continuously changing fractions (Bhattacharya, 2003; Seiner et al., 2011; Stupkiewicz et al., 2007). To solve this inconsistency, some compatibility analyses are performed in the following section.

#### 4. Compatibility analysis and discussion

Here, the compatibility analysis is focused on the twin boundary and the A-M interface (phase boundary), i.e., the coherent interfaces between the cubic austenite phase and the tetragonal martensite variants. Strictly speaking, the 10M martensite phase of the ferromagnetic shape memory alloy Ni-Mn-Ga are slightly monoclinic: its characteristic angle  $\gamma = 90.37^\circ$  is not exactly equal to  $90^\circ$  of a tetragonal lattice (Chulist et al., 2013; Heczko et al., 2013; Sozinov et al., 2011; Straka et al., 2011). To simplify the analysis, the Austenite-to-10M martensite transition in Ni-Mn-Ga is approximated by a cubic-to-tetragonal transition. Three tetragonal martensite variants ( $M_1$ ,  $M_2$  and  $M_3$  with short axis  $b$  along  $y$ ,  $x$  and  $z$  directions respectively) can be formed and their corresponding Bain matrices (Bhattacharya, 2003) are:

$$\mathbf{U}_1 = \begin{pmatrix} \alpha & 0 & 0 \\ 0 & \beta & 0 \\ 0 & 0 & \alpha \end{pmatrix}, \quad \mathbf{U}_2 = \begin{pmatrix} \beta & 0 & 0 \\ 0 & \alpha & 0 \\ 0 & 0 & \alpha \end{pmatrix} \quad \text{and} \quad \mathbf{U}_3 = \begin{pmatrix} \alpha & 0 & 0 \\ 0 & \alpha & 0 \\ 0 & 0 & \beta \end{pmatrix} \quad (1)$$

where  $\alpha = \frac{a}{a_0} = 1.0188$  and  $\beta = \frac{c}{a_0} = 0.9606$  for the material (the meaning and the values of the lattice parameters  $a_0$ ,  $a$  and  $c$  have been given in Section 2).

Firstly, we check the formation of the compatible twin boundaries among the three variants:  $M_1$ ,  $M_2$  and  $M_3$ . The kinematic compatibility condition between two unstressed, but possibly rotated, martensite variants can be formulated into a twinning equation (Bhattacharya, 2003):

$$\mathbf{R}\mathbf{U}_I - \mathbf{U}_J = \mathbf{a} \otimes \mathbf{n}, \quad (2)$$

where  $\mathbf{U}_I$  and  $\mathbf{U}_J$  are the Bain matrices of the  $I^{\text{th}}$  and the  $J^{\text{th}}$  martensite variants;  $\mathbf{R}$  belonging to a 3D rotation group ( $SO(3)$ ) represents the rotation of the variant  $\mathbf{U}_I$  with respect to the variant  $\mathbf{U}_J$  when the twin is formed;  $\mathbf{a} \otimes \mathbf{n}$  is a dyadic product of a non-zero vector  $\mathbf{a}$  and a unit vector  $\mathbf{n}$ ; the vector  $\mathbf{n}$  represents the normal of the twinning plane in the reference cubic coordinate system while the vector  $\mathbf{a}$  is the so-called shearing vector.

Following the standard solving method (Bhattacharya, 2003), the solution to the twinning equation Eq. (2) with the Bain matrices in Eq. (1) can be found. There are three types of twins: (1) the twin boundaries (planes) between the variant-pair  $M_1:M_2$  have the normal vector  $\mathbf{n} = [\pm 1 \pm 1 \ 0]$ , cutting the  $x$ - $y$  plane (the experimentally observed specimen surface) by an angle  $45^\circ$  as shown in Fig. 5, where the observed surface in  $x$ - $y$  plane is highlighted in light blue and dark blue schematically representing the two variants observed in the surface; (2) the twin boundaries between the variant-pair  $M_2:M_3$  have the normal vector  $\mathbf{n} = [\pm 1 \ 0 \pm 1]$ , cutting the  $x$ - $y$  plane with a horizontal line (Fig. 5); (3) the twin boundaries between the variant-pair  $M_1:M_3$  have the normal vector  $\mathbf{n} = [0 \pm 1 \pm 1]$ , cutting the  $x$ - $y$  plane with a vertical line (Fig. 5).

Based on the comparison between the above theoretically predicted twin boundaries (Fig. 5) and the experimentally observed twin boundary in Fig. 3 whose twin plane cuts the  $x$ - $y$  plane (the observed specimen surface) by the



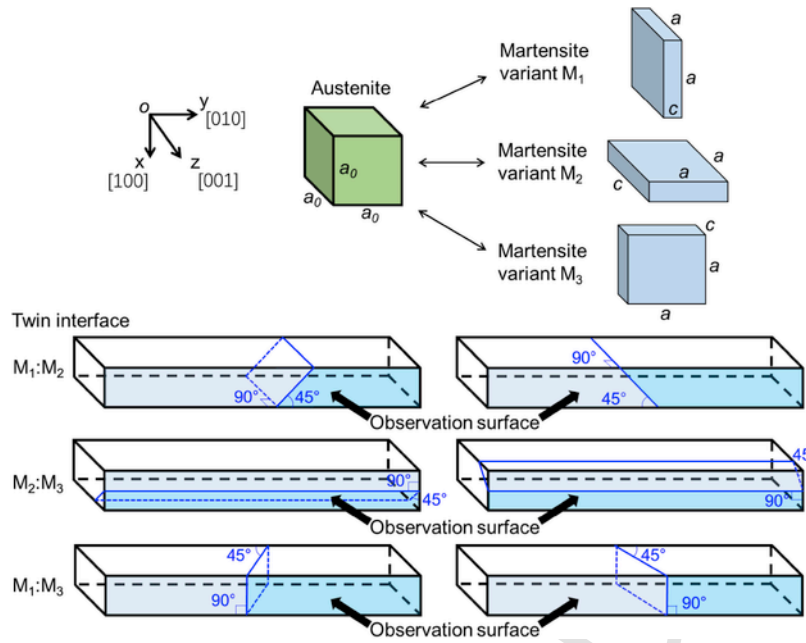


Fig. 5. Twin boundaries of the tetragonal martensite variants of Ni-Mn-Ga. The x-y plane (the experimentally observed surface) is shown in color in each 3D schematic, where different colors represent different variants. (For interpretation of the references to color in this figure legend, the reader is referred to the Web version of this article.)

angle  $44.7^\circ$ , it is easy to confirm that the martensite reorientation under the magnetic field (along x-direction) and the compressive force (along y-direction) in the dynamic tests (Fig. 1) is the cyclic transition between the variant-pair  $M_1:M_2$ .

Then, we check whether the twin ( $M_1:M_2$ ) can be compatible with the cubic A-phase via the habit plane equation for the Austenite-Martensite interface (A-M interface) (Bhattacharya, 2003):

$$\mathbf{R}'(f\mathbf{R}\mathbf{U}_I + (1-f)\mathbf{U}_J) - \mathbf{I} = \mathbf{b} \otimes \mathbf{m}. \quad (3)$$

where  $\mathbf{I}$  is an identity second-order tensor representing the Bain matrix of the A-phase;  $\mathbf{m}$  is the normal of the A-M interface while the vector  $\mathbf{b}$  is the shear vector;  $\mathbf{R}$  represents the rotation of the martensite twin (consisting of the  $I^{\text{th}}$  and the  $J^{\text{th}}$  martensite variants) with respect to the A-phase;  $f$  and  $1-f$  are the fractions of the  $I^{\text{th}}$  and the  $J^{\text{th}}$  martensite variants in the twin, respectively. Equation (3) represents the kinematic compatibility between undeformed austenite and a martensite twin.

Solving Eq. (3) with the twin  $M_1:M_2$ , we can obtain the normal of the compatible A-M interface (the vector  $\mathbf{m}$ ) and the corresponding volume fraction  $f$  of variant  $M_1$  in the twin as listed in Table 1. The normal of the compatible A-M interface has several possibilities for the material:

$$\mathbf{m}^\pm = \frac{1}{1.4518} [\pm 1.0519, \pm 0.0367, 1] \quad \text{or} \quad \mathbf{m}^\pm = \frac{1}{1.4518} [\pm 0.0367, \pm 1.0519, 1] \quad (4)$$

Table 1

Theoretical prediction on the compatible interfaces between the austenite phase and the martensite twins  $M_1:M_2$ .

Martensite variant-pair	$f$ (fraction of $M_1$ )	$n$ (normal of fine-twins)	$m$ (normal of A-M interface)
$M_1:M_2$	0.32	[1 1 0]	1/1.4518 [-1.0519 0.0367 1]
		[1 1 0]	1/1.4518 [1.0519 -0.0367 1]
		[-1 1 0]	1/1.4518 [1.0519 0.0367 1]
		[-1 1 0]	1/1.4518 [-1.0519 -0.0367 1]
	0.68	[1 1 0]	1/1.4518 [0.0367 -1.0519 1]
		[1 1 0]	1/1.4518 [-0.0367 1.0519 1]
		[-1 1 0]	1/1.4518 [0.0367 1.0519 1]
		[-1 1 0]	1/1.4518 [-0.0367 -1.0519 1]

It is seen from Eq. (4) that one of the absolute values of the components of the normal is 0.0367, which is much smaller than those of the other two components (1.0519 and 1), and the two components (1.0519 and 1) are very close to each other. So, the orientation of the A-M interface can be approximated as

$$\mathbf{m} = \left(1/\sqrt{2}\right) [\pm 1, 0, 1] \quad \text{or} \quad \left(1/\sqrt{2}\right) [0, \pm 1, 1] \quad (5)$$

The A-M interface with the normal  $\mathbf{m}$  in Eq. (5) can cut the x-y plane (the experimentally observed surface) by a horizontal line or a vertical line, depending on the volume fraction  $f$  as shown in Fig. 6(a) and (b). Such theoretical prediction doesn't agree with the experimental observation in Fig. 2(b) where the A-M interface cuts the x-y plane by an angle close to 45°.

In order to find out the reason for this inconsistency, we also solve the habit-plane equation (Eq. (3)) between A-phase and other kinds of twins to determine other possible A-M interfaces, i.e., the compatible interface between A-phase and other martensite twins such as the twins  $M_1:M_3$  and  $M_2:M_3$ . Following the similar solving procedures, all the possible A-M interfaces are determined and listed in Table 2, and the corresponding traces in the observed surface (i.e., the intersection line of the A-M interface in the x-y plane) are shown in Fig. 6(a)~(f). It is seen that the traces of the A-M interfaces in Fig. 6(d) and (f) have the angle 45°. So the twin  $M_1:M_3$  (with the fixed volume fractions 68%:32%) and the twin  $M_2:M_3$  (with the fixed volume fractions 68%:32%) can have a compatible A-M interface with the trace in x-y plane agreeing with the experimental observation (of 45° angle).

Combining the calculations above and the observations in the experiments, we can conjecture that the interface between the active M-zone (M-phase of the cyclic switching between variants  $M_1$  and  $M_2$ ) and the non-active A-zone (A-phase) is not a simple sharp interface, but a transitional layer containing the twins  $M_1:M_3$  or  $M_2:M_3$ . The situations about the transitional layer at the interfacial zone were studied in the literature to explain the coexistence of different phases; for example, some needle twin structures have been observed (Boullay et al., 2001; Chu, 1993; Zárubová et al., 2010) and modeled (James et al., 1995; Li, 2001; Schryvers et al., 2002; Seiner et al., 2011) in similar materials (Cu-Al-Ni and Ni-Al), where the gradually tapering needle twins are reported to serve as a compatible transition layer between A-phase and M-phase (no matter single variant state or twinned martensite). Inspired by such needle twin microstructure, the compatible interfacial zone between the active M-zone and the non-active A-zone can be schematically drawn in Fig. 7(a)~(c), where Fig. 7(a) shows the 3D schematic and Fig. 7(b) and (c) show the unfolded views of the possible horizontal and vertical needle twin structures of the martensite variant  $M_3$ , respectively.

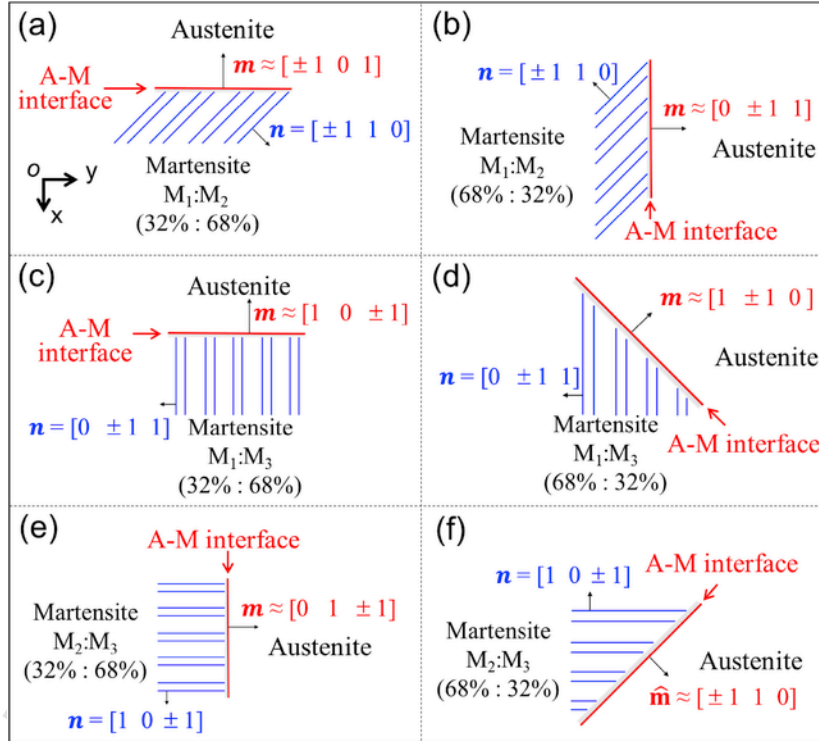


Fig. 6. Theoretical predictions of all the possible patterns of A-M interface and martensite fine-twins (projections on x-y plane). The patterns in (a) and (b) are formed by fine twins of  $M_1:M_2$ , (c) and (d) are formed by fine twins of  $M_1:M_3$ , (e) and (f) are formed by fine twins of  $M_2:M_3$ .

**Table 2**

Theoretical prediction on the compatible interfaces between the austenite phase and the martensite twins, whose schematic microstructure patterns are given in Fig. 6.

Martensite variant-pair $M_i:M_j$	$f$ (fraction of $M_i$ )	$n$ (normal of fine-twins)	$m$ (normal of A-M interface)	Trace of A-M interface (on observation surface)
$M_1:M_2$	0.32	$[1\ 1\ 0]$ $[-1\ 1\ 0]$	$1/\sqrt{2} [\pm 1\ 0\ 1]$ $1/\sqrt{2} [\pm 1\ 0\ 1]$	horizontal (Fig. 6(a))
	0.68	$[1\ 1\ 0]$ $[-1\ 1\ 0]$	$1/\sqrt{2} [0\ \pm 1\ 1]$ $1/\sqrt{2} [0\ \pm 1\ 1]$	vertical (Fig. 6(b))
$M_1:M_3$	0.32	$[0\ 1\ 1]$ $[0\ -1\ 1]$	$1/\sqrt{2} [1\ 0\ \pm 1]$ $1/\sqrt{2} [1\ 0\ \pm 1]$	horizontal (Fig. 6(c))
	0.68	$[0\ 1\ 1]$ $[0\ -1\ 1]$	$1/\sqrt{2} [1\ \pm 1\ 0]$ $1/\sqrt{2} [1\ \pm 1\ 0]$	45° (Fig. 6(d))
$M_2:M_3$	0.32	$[1\ 0\ 1]$ $[1\ 0\ -1]$	$1/\sqrt{2} [0\ 1\ \pm 1]$ $1/\sqrt{2} [0\ 1\ \pm 1]$	vertical (Fig. 6(e))
	0.68	$[1\ 0\ 1]$ $[1\ 0\ -1]$	$1/\sqrt{2} [\pm 1\ 1\ 0]$ $1/\sqrt{2} [\pm 1\ 1\ 0]$	45° (Fig. 6(f))

In order to clarify the microstructure of the interfacial zone in the current specimen (details of the interfacial zone cannot be resolved in the high-frequency actuation due to the limited resolution), we performed a simple test: by quasi-static mechanical compressions along  $y$  and  $x$  directions, we created twins consisting  $M_1$  and  $M_2$  in the specimen (with the same orientation as that in the dynamic case of the high-frequency magneto-mechanical loading); then, a hot airflow was forced to pass through the specimen to increase the specimen temperature, and an optical microscope with a polarized light (Olympus AX70) was used to observe the specimen surface ( $x$ - $y$  plane) as shown in Fig. 7(d) where there is a horizontal needle zone (the interfacial zone) separating the martensite zone (45° twins between  $M_1$  and  $M_2$ ) from the A-phase, which is similar to the previously reported needle patterns observed in Cu-Al-Ni and Ni-Al (Boullay et al., 2001; Chu, 1993; Zárubová et al., 2010). Moreover, it is noted that the A-M interface is parallel to the twin boundaries at the observed specimen surface in Fig. 7(d), which is consistent with that in the dynamic experiment as shown in Fig. 4. Therefore, the experimentally observed compatible A-M interface in the dynamic experiment in Fig. 4 can be due to the occurrence of the transition needles of the variant  $M_3$  (horizontal needles in Fig. 7(b) or vertical ones in Fig. 7(c)). It means, to reach the compatibility between austenite and martensite zones, the third martensite variant  $M_3$  must be nucleated besides the original martensite variants  $M_1$  and  $M_2$  taking part in the cyclic martensite reorientation during the dynamic loading. Further higher resolution observation on the fine twin structures at the interfacial zone may help better understand the dynamic behaviors.

In summary, when the temperature-induced phase transformation occurs during the high-frequency field-induced martensite reorientation, the specimen is divided into three zones as schematically shown in Fig. 8(a): the **non-active Austenite zone** (A-zone with the constant local strain), the **active Martensite zone** (M-zone of the cyclic switching between the variants  $M_1$  and  $M_2$ ) and the **buffering needle zone** (interfacial zone) with the fine transition needles of the variant  $M_3$  which helps maintain the compatibility between A-zone with constant deformation and M-zone with cyclic martensite reorientation during the dynamic loading. When the ambient airflow increases, the non-active A-zone shrinks and the active M-zone expands through the propagation of the A-M phase boundary (see Fig. 8(a) ~ 8(c)); if the airflow is strong enough to keep the specimen temperature lower than the phase-transformation temperature, the specimen would be fully occupied by the active martensite zone and the output strain reaches the maximum value (around 6% in current system).

## 5. Summary and conclusions

In this paper, we report a test of the high-frequency magnetic-field-induced martensite reorientation in Ni-Mn-Ga ferromagnetic shape memory alloy under stepped changing ambient airflows with the in-situ optical observation on the specimen surface, from which the local strain evolution (DIC strain maps) and the associated transformation/reorientation among the various phases/variants in the thermo-magneto-mechanical situations are demonstrated. It is shown that the high-frequency frictional martensite reorientation causes a significant temperature rise leading to the temperature-induced Martensite-to-Austenite phase transformation; i.e., some part of the specimen becomes austenite phase which doesn't contribute any cyclic deformation in current low-level magnetic loading so that the global field-induced deformation is significantly reduced. Increasing heat transfer to ambient by controlling the ambient airflow is

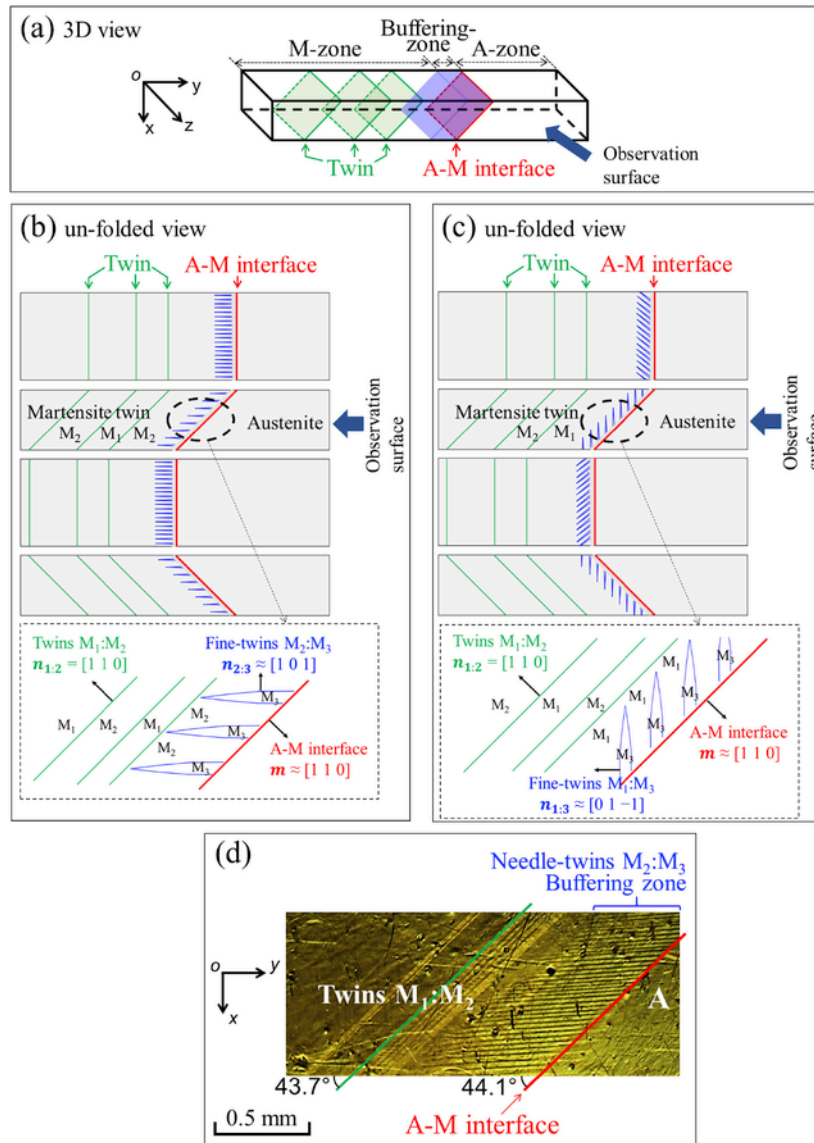


Fig. 7. The 3D and unfolded schematics and of the compatible microstructures with the coexistence of non-active austenite zone, buffering needle zone and active martensite zone in (a)~(c); (d) The optical observation of the needle fine twins jointly generated with A-M interface in a quasi-static thermo-mechanical test.

demonstrated to be an effective way to reduce the influence of the austenite phase: the volume size of austenite phase reduces with increasing the ambient airflow. That presents a novel mechanism: the temperature-induced phase transformation (phase boundary motion) and the field-induced martensite reorientation (twin boundary motion) coexist in the magnetic actuation with changing ambient airflow, as the specimen needs to self-organize the different phases/variants to satisfy all the thermo-magneto-mechanical boundary conditions. The self-organized microstructure of the different phases/variants can be understood by compatibility analysis. The main conclusions can be drawn:

- (1) The coexistence of the temperature-induced phase transformation and the field-induced martensite reorientation divides the specimen into three zones: the **non-active austenite zone** (A-zone, not sensitive to the applied low-level magnetic field), the **active martensite zone** (M-zone, taking cyclic martensite reorientation to provide strain oscillation) and the buffering zone (the interfacial zone with needle twins between the A- and M-zones). To be compatible with both the active zone and the non-active zone, the interfacial zone might need the needle twin structure formation composed of the third martensite variant which does not participate in the martensite reorientation; i.e., the martensite variant which does not exist originally in the field-induced deformation can be gen-

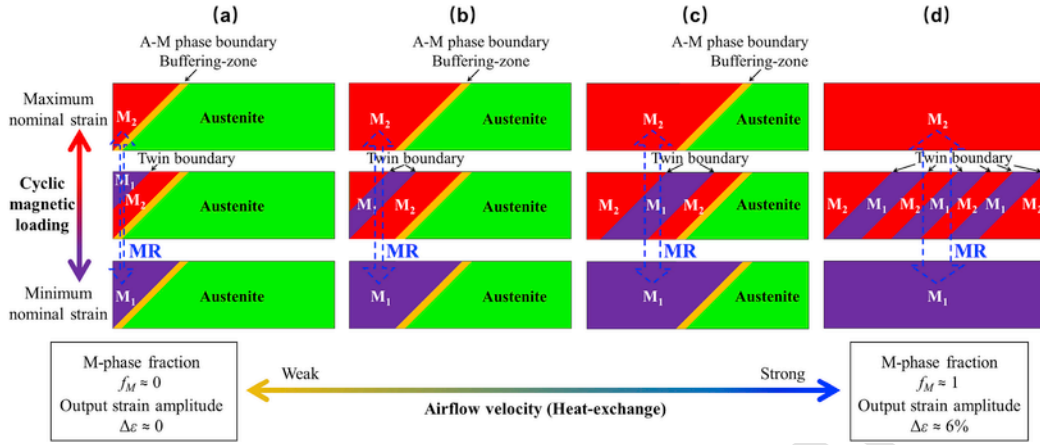


Fig. 8. Schematic of the martensite reorientation (with twin boundary motion) between  $M_1$  and  $M_2$  driven by cyclic magneto-mechanical loading (see the vertical evolution, marked by vertical dashed double-headed arrows) and the phase transformation (with A-M phase boundary motion) driven by changing heat-exchange efficiency (see the horizontal evolution from (a) to (d)). The buffering zone can be compatible with both the austenite phase and martensite phase (no matter single variant or twins of  $M_1$  and  $M_2$ ).

erated due to the requirement of the compatibility between the active martensite zone and the non-active austenite zone.

- (2) By controlling the ambient heat-transfer efficiency (changing ambient airflow velocity), the volume fractions of the active martensite zone and non-active austenite zone in the specimen under the low-level magnetic field loading can be self-organized to maintain the heat balance. Therefore, the global output strain amplitude can be significantly tuned (from  $\sim 1\%$  to  $\sim 6\%$  in the current study) while the working temperature keeps almost constant at the material characteristic phase transformation temperature  $M_s$  and  $M_f$ .

## Acknowledgment

Shaobin Zhang would like to acknowledge China Scholarship Council (CSC) for the financial support (No. 201506280009).

## Appendix A.

To measure the characteristic transformation temperatures of the material used in our experiment, Differential Scanning Calorimetry (DSC) test was performed in a temperature range between  $30^\circ\text{C}$  and  $55^\circ\text{C}$  (by a machine of DSC131 supplied by SETARAM Instrumentation). The heating/cooling rate of the test is  $0.5^\circ\text{C}/\text{min}$  and the weight of the sample is  $50.1\text{ mg}$ . The obtained heat flow curve is shown in Fig. A1, from which the material characteristic transformation temperatures  $M_s$ ,  $M_f$ ,  $A_s$  and  $A_f$  were found to be  $36.5^\circ\text{C}$ ,  $35.5^\circ\text{C}$ ,  $41.5^\circ\text{C}$  and  $42.2^\circ\text{C}$ , respectively.

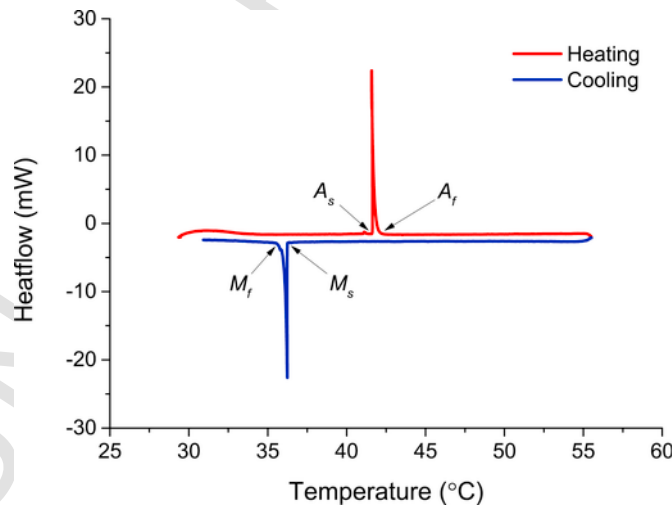




Fig. A1. DSC curve of the single crystal Ni-Mn-Ga at the heating/cooling rate of 0.5 °C/min.

## References

- Arndt, M., Griebel, M., Novák, V., Roubíček, T., Šittner, P., 2006. Martensitic transformation in NiMnGa single crystals: numerical simulation and experiments. *Int. J. Plast.* 22, 1943–1961. <https://doi.org/10.1016/j.ijplas.2006.03.001>.
- Basso, V., 2011. The magnetocaloric effect at the first-order magneto-elastic phase. *J. Phys. Condens. Matter* 226004. <https://doi.org/10.1088/0953-8984/23/22/226004>.
- Bhattacharya, K., 2003. *Microstructure of Martensite: Why it Forms and How it Gives Rise to the Shape-memory Effect*. Oxford University Press.
- Boullay, P., Schryvers, D., Kohn, R.V., 2001. Bending martensite needles in  $\text{Ni}_{65}\text{Al}_{35}$  investigated by two-dimensional elasticity and high-resolution transmission electron microscopy. *Phys. Rev. B* 64, 1–8. <https://doi.org/10.1103/PhysRevB.64.144105>.
- Bruno, N.M., Wang, S., Karaman, I., Chumlyakov, Y.I., 2016. Reversible martensitic transformation under low magnetic fields in magnetic shape memory alloys. *Sci. Rep.* 7, 40434. <https://doi.org/10.1038/srep40434>.
- Chen, X., Srivastava, V., Dabade, V., James, R.D., 2013. Study of the cofactor conditions: conditions of supercompatibility between phases. *J. Mech. Phys. Solids* 61, 2566–2587. <https://doi.org/10.1016/j.jmps.2013.08.004>.
- Chmielus, M., Chernenko, V.A., Knowlton, W.B., Kistorz, G., Müllner, P., 2008. Training, constraints, and high-cycle magneto-mechanical properties of Ni-Mn-Ga magnetic shape-memory alloys. *Eur. Phys. J. Spec. Top.* 158, 79–85. <https://doi.org/10.1140/epjst/e2008-00657-3>.
- Chu, C.-H., 1993. *Hysteresis and Microstructures: a Study of Biaxial Loading on Compound Twins of Copper-aluminum-nickel Single Crystals*. PhD thesis University of Minnesota, USA.
- Chulist, R., Straka, L., Lanska, N., Soroka, A., Sozinov, A., Skrotzki, W., 2013. Characterization of mobile type I and type II twin boundaries in 10M modulated Ni-Mn-Ga martensite by electron backscatter diffraction. *Acta Mater.* 61, 1913–1920. <https://doi.org/10.1016/j.actamat.2012.12.012>.
- Ge, Y., Heczko, O., Soderberg, O., Hannula, S.P., Lindroos, V.K., 2005. Investigation of magnetic domains in Ni-Mn-Ga alloys with a scanning electron microscope. *Smart Mater. Struct.* 14, S211–S215. <https://doi.org/10.1088/0964-1726/14/5/007>.
- Glavatska, N., Mogilyny, G., Glavatskiy, I., Gavriljuk, V., 2002. Temperature stability of martensite and magnetic field induced strain in Ni-Mn-Ga. *Scr. Mater.* 46, 605–610. [https://doi.org/10.1016/S1359-6462\(02\)00019-2](https://doi.org/10.1016/S1359-6462(02)00019-2).
- Haldar, K., Lagoudas, D.C., Karaman, I., 2014. Magnetic field-induced martensitic phase transformation in magnetic shape memory alloys: modeling and experiments. *J. Mech. Phys. Solids* 69, 33–66. <https://doi.org/10.1016/j.jmps.2014.04.011>.
- Heczko, O., Lanska, N., Soderberg, O., Ullakko, K., 2002. Temperature variation of structure and magnetic properties of Ni-Mn-Ga magnetic shape memory alloys. *J. Magn. Magn. Mater.* 242–245, 1446–1449. [https://doi.org/10.1016/S0304-8853\(01\)01087-3](https://doi.org/10.1016/S0304-8853(01)01087-3).
- Heczko, O., Sozinov, A., Ullakko, K., 2000. Giant field-induced reversible strain in magnetic shape memory NiMnGa alloy. *IEEE Trans. Magn.* 36, 3266–3268. <https://doi.org/10.1109/20.908764>.
- Heczko, O., Straka, L., Seiner, H., 2013. Different microstructures of mobile twin boundaries in 10 M modulated Ni-Mn-Ga martensite. *Acta Mater.* 61, 622–631. <https://doi.org/10.1016/j.actamat.2012.10.007>.
- Henry, C.P., 2002. *Dynamic Actuation Properties of Ni-mn-Ga Ferromagnetic Shape Memory Alloys*. PhD thesis Massachusetts Institute of Technology, USA.
- James, R.D., Kohn, R.V., Shield, T.W., 1995. Modeling of branched needle microstructures at the edge of a martensite laminate. *Le J. Phys. IV* 5, C8-253–C8-259.
- Jugo, J., Feuchtwaenger, J., Corres, J., Etxebarria, V., 2017. Analysis of temperature effects in high accuracy ferromagnetic shape memory alloy actuators. *Sensor Actuator A Phys.* <https://doi.org/10.1016/j.sna.2017.11.049>.
- Karaca, H., Karaman, I., Basaran, B., Chumlyakov, Y., Maier, H., 2006. Magnetic field and stress induced martensite reorientation in NiMnGa ferromagnetic shape memory alloy single crystals. *Acta Mater.* 54, 233–245. <https://doi.org/10.1016/j.actamat.2005.09.004>.
- Karaca, H.E., Karaman, I., Basaran, B., Lagoudas, D.C., Chumlyakov, Y.I., Maier, H.J., 2007. On the stress-assisted magnetic-field-induced phase transformation in  $\text{Ni}_2\text{MnGa}$  ferromagnetic shape memory alloys. *Acta Mater.* 55, 4253–4269. <https://doi.org/10.1016/j.actamat.2007.03.025>.
- Karaca, H.E., Karaman, I., Basaran, B., Ren, Y., Chumlyakov, Y.I., Maier, H.J., 2009. Magnetic field-induced phase transformation in NiMnCoIn magnetic shape-memory alloys—a new actuation mechanism with large work output. *Adv. Funct. Mater.* 19, 983–998. <https://doi.org/10.1002/adfm.200801322>.
- Lai, Y.W., 2009. *Magnetic Microstructure and Actuation Dynamics of NiMnGa Magnetic Shape Memory Materials*. PhD thesis Technische Universität Dresden, Germany.
- Lai, Y.W., Schafer, R., Schultz, L., McCord, J., 2008. Direct observation of AC field-induced twin-boundary dynamics in bulk NiMnGa. *Acta Mater.* 56, 5130–5137. <https://doi.org/10.1016/j.actamat.2008.06.030>.
- Li, Z., 2001. Computations of needle-like microstructures. *Appl. Numer. Math.* 39, 1–15. [https://doi.org/10.1016/S0168-9274\(01\)00032-0](https://doi.org/10.1016/S0168-9274(01)00032-0).
- Li, Z., Zhang, Y., Sánchez-Valdés, C.F., Llamazares, J.L.S., Esling, C., Zhao, X., Zuo, L., 2014. Giant magnetocaloric effect in melt-spun Ni-Mn-Ga ribbons with magneto-multistructural transformation. *Appl. Phys. Lett.* 104, <https://doi.org/10.1063/1.4863273>.
- Murray, S.J., Marioni, M., Allen, S.M., O'Handley, R.C., Logrosso, T.A., 2000. 6% magnetic-field-induced strain by twin-boundary motion in ferromagnetic Ni–Mn–Ga. *Appl. Phys. Lett.* 77, 886–888. <https://doi.org/10.1063/1.1306635>.
- Pagounis, E., Chulist, R., Szczerba, M.J., Laufenberg, M., 2014. Over 7% magnetic field-induced strain in a Ni-Mn-Ga five-layered martensite. *Appl. Phys. Lett.* 105, 1–5. <https://doi.org/10.1063/1.4892633>.
- Pascan, O.-Z., 2015. *Dynamic Behaviors of Ferromagnetic Shape Memory Alloys*. PhD thesis ENSTA-ParisTech, France.
- Pascan, O.-Z., He, Y.J., Moumni, Z., Zhang, W.H., 2015. Temperature rise of high-frequency martensite reorientation via Type II twin boundary motion in NiMnGa ferromagnetic shape memory alloy. *Scr. Mater.* 104, 71–74. <https://doi.org/10.1016/j.scriptamat.2015.04.006>.
- Pinneker, V., Guelting, M., Sozinov, A., Kohl, M., 2014. Single phase boundary actuation of a ferromagnetic shape memory foil. *Acta Mater.* 64, 179–187. <https://doi.org/10.1016/j.actamat.2013.10.025>.
- Pinneker, V., Yin, R., Eberl, C., Sozinov, A., Ezer, Y., Kohl, M., 2013. Evolution of local strain bands of different orientation in single crystalline Ni-Mn-Ga foils under tension. *J. Alloy. Comp.* 577, S358–S361. <https://doi.org/10.1016/j.jallcom.2012.03.004>.

- Rogovoy, A., Stolbova, O., 2016. Modeling the magnetic field control of phase transition in ferromagnetic shape memory alloys. *Int. J. Plast.* 85, 130–155. <https://doi.org/10.1016/j.ijplas.2016.07.006>.
- Schryvers, D., Boullay, P., Potapov, P.L., Kohn, R.V., Ball, J.M., 2002. Microstructures and interfaces in Ni-Al martensite: comparing HRTEM observations with continuum theories. *Int. J. Solid Struct.* 39, 3543–3554. [https://doi.org/10.1016/S0020-7683\(02\)00167-1](https://doi.org/10.1016/S0020-7683(02)00167-1).
- Sehitoglu, H., Wang, J., Maier, H.J., 2012. Transformation and slip behavior of Ni<sub>2</sub>FeGa. *Int. J. Plast.* 39, 61–74. <https://doi.org/10.1016/j.ijplas.2012.05.011>.
- Seiner, H., Glatz, O., Landa, M., 2011. A finite element analysis of the morphology of the twinned-to-detwinned interface observed in microstructure of the Cu-Al-Ni shape memory alloy. *Int. J. Solid Struct.* 48, 2005–2014. <https://doi.org/10.1016/j.ijsolstr.2011.03.007>.
- Singh, S., Souza, S.W.D., Mukherjee, K., Kushwaha, P., Barman, S.R., Agarwal, S., Chakrabarti, A., Sampathkumaran, E.V., 2014. Magnetic properties and magnetocaloric effect in Pt doped Ni-Mn-Ga. *Appl. Phys. Lett.* 231909. <https://doi.org/10.1063/1.4883404>.
- Smith, A.R., Tellinen, J., Ullakko, K., 2014. Rapid actuation and response of Ni-Mn-Ga to magnetic-field-induced stress. *Acta Mater.* 80, 373–379. <https://doi.org/10.1016/j.actamat.2014.06.054>.
- Sokolovskiy, V., Grünebohm, A., Buchelnikov, V., Entel, P., 2014. Ab initio and Monte Carlo approaches for the magnetocaloric effect in Co- and in-doped Ni-Mn-Ga heusler alloys. *Entropy* 16, 4992–5019. <https://doi.org/10.3390/e16094992>.
- Song, Y., Chen, X., Dabade, V., Shield, T.W., James, R.D., 2013. Enhanced reversibility and unusual microstructure of a phase-transforming material. *Nature* 502, 85–88. <https://doi.org/10.1038/nature12532>.
- Sozinov, A., Lanska, N., Soroka, A., Straka, L., 2011. Highly mobile type II twin boundary in Ni-Mn-Ga five-layered martensite. *Appl. Phys. Lett.* 99, 124103. <https://doi.org/10.1063/1.3640489>.
- Straka, L., Heczko, O., Hänninen, H., 2008. Activation of magnetic shape memory effect in Ni-Mn-Ga alloys by mechanical and magnetic treatment. *Acta Mater.* 56, 5492–5499. <https://doi.org/10.1016/j.actamat.2008.07.020>.
- Straka, L., Heczko, O., Hannula, S.P., 2006. Temperature dependence of reversible field-induced strain in Ni-Mn-Ga single crystal. *Scr. Mater.* 54, 1497–1500. <https://doi.org/10.1016/j.scriptamat.2005.12.046>.
- Straka, L., Heczko, O., Seiner, H., Lanska, N., Drahoukoupil, J., Soroka, A., Fähler, S., Hänninen, H., Sozinov, A., 2011. Highly mobile twinned interface in 10M modulated Ni-Mn-Ga martensite: analysis beyond the tetragonal approximation of lattice. *Acta Mater.* 59, 7450–7463. <https://doi.org/10.1016/j.actamat.2011.09.020>.
- Stupkiewicz, S., Maciejewski, G., Petryk, H., 2007. Low-energy morphology of the interface layer between austenite and twinned martensite. *Acta Mater.* 55, 6292–6306. <https://doi.org/10.1016/j.actamat.2007.07.034>.
- Techapiesancharoenkij, R., Kostamo, J., Allen, S.M., O'Handley, R.C., 2009. Frequency response of acoustic-assisted Ni-Mn-Ga ferromagnetic-shape-memory-alloy actuator. *J. Appl. Phys.* 105, 93923. <https://doi.org/10.1063/1.3125307>.
- Yin, R., Wendler, F., Krevet, B., Kohl, M., 2016. A magnetic shape memory microactuator with intrinsic position sensing. *Sensor Actuator A Phys.* 246, 48–57. <https://doi.org/10.1016/j.sna.2016.05.013>.
- Zárubová, N., Gemperlová, J., Gemperle, A., Dlabáček, Z., Šittner, P., Novák, V., 2010. In situ TEM observation of stress-induced martensitic transformations and twinning processes in CuAlNi single crystals. *Acta Mater.* 58, 5109–5119. <https://doi.org/10.1016/j.actamat.2010.05.046>.
- Zhang, S., Chen, X., Moumni, Z., He, Y., 2018. Thermal effects on high-frequency magnetic-field-induced martensite reorientation in ferromagnetic shape memory alloys: an experimental and theoretical investigation. *Int. J. Plast.* <https://doi.org/10.1016/j.ijplas.2018.04.008>, Accepted.